AIAA JOURNAL
Vol. 48, No. 9, September 2010

Effects of Evaporating Droplets on Shock Waves

James Kersey*
Gamma Technologies, Inc., Westmont, Illinois 60559
Eric Loth†
University of Virginia, Charlottesville, Virginia 22904
and
Dennis Lankford‡
Aerospace Testing Alliance, Tullahoma, Tennessee 37388

DOI: 10.2514/1.J050162

A methodology for simulating two-way multiphase coupling of mass, momentum, and energy was developed to investigate the effect of droplet mass and heat transfer on one-dimensional shock waves. The numerical approach employed a conservative formulation for the gas and a Lagrangian formulation for the particles. The approach was verified for one-way heat transfer, evaporation and condensation for low-speed flows, and for two-way shock attenuation for solid particles and small evaporating drops (for which breakup is not expected and internal temperature gradients are weak). Parametric studies were conducted to investigate the coupling physics, and, surprisingly, finite rate evaporation and two-way coupling were found to increase the rate of shock attenuation and reduce the postshock gas temperature for mass loadings as small as 0.5%. Larger drops led to long regions of nonequilibrium as did, unexpectedly, effects of evaporation.

I. Introduction

DISPERSED multiphase flows, whose particle volume fractions are less than 10%, are important scientifically and in many industrial, automotive, and aerospace engineering systems. This includes circulating fluidized beds for power generation, fuel sprays in internal combustion engines, and aircraft wing and engine inlet icing. In such cases, the mass, momentum, and energy interactions between particles or drops and a gas flow can be significant. This is particularly true for the case of fuel spray injection into high-speed propulsion concepts such as scramjets for which interaction between shock waves and evaporating, combusting droplets is an important area of study. Because of this, there have been several experimental and numerical studies that examined the attenuation effects of interphase momentum and kinetic energy transfer on shock waves for solid and liquid particles.

While studies that consider effects of evaporation on shock physics are rare, a number of experimental and computational studies have investigated either the phase change in the relaxation zone behind a shock or the shock attenuation due to solid-particle interaction. For example, early numerical studies of phase change in the relaxation zone behind a shock of fixed strength were reported by Lu and Chiu [1] and by Panton and Oppenheim [2]. Both of these studies solved 1-D conservation equations using an Eulerian formulation for the gas and liquid phases and found that both condensation and evaporation may occur behind a shock driven primarily by the partial pressure gradient. Panton and Oppenheim conducted systematic parametric studies of factors influencing temperatures, velocities and mass transfer rates. Goossens et al. [3] used experimental and theoretical techniques to examine the effect of shock waves on evaporation, but shock decay was not studied. Sommerfeld [4] conducted experimental and numerical studies of shock attenuation by solid-particle flows. Haylett et al. [5] discussed shock-tube measurement of evaporating liquids, some including ignition (e.g., Hanson et al. [6]). For solid (nonevaporating) particles, numerical simulations were conducted by Sivier et al. [7] and Haselbacher et al. [8] for which shock attenuation compared well with the experimental results of Sommerfeld [4]. The most relevant previous numerical work found was that by Chang and Kailasanath [9], which considered relatively large droplets interacting with a shock wave. However, their study assumed instantaneous droplet breakup and evaporation as soon as the shock impacted and thus did not examine effects of evaporation rate or particle inertia on shock attenuation or effects of finite rate evaporation, mass loading, and particle size.

The current numerical work examines in detail shock interactions with evaporating droplets in a parametric fashion and is the first study to do so with respect to finite mass and heat transfer effects on the coupled shock physics and attenuation. The focus herein is on the interaction of moderate strength shocks with small drops, e.g., 20 μm or less, in a nonreacting flow consistent with the conditions of Goossens et al. [3]. As such, droplet breakup, combustion, and internal temperature gradients are neglected. Since such aspects are important to propulsion systems, they should be considered in future studies.

II. Methodology

A. Inviscid Gas-Phase Equations

The governing equations for the continuous phase, assuming inviscid compressible flow, can be written as a coupled set of conservative partial differential equations of the general form:

$$\frac{\partial \mathbf{U}}{\partial t} + \frac{\partial \mathbf{F}_j}{\partial x_j} = \mathbf{S} \tag{1}$$

Here, summation notation is used and the left-hand side is defined by the vectors

$$\mathbf{U} = \begin{bmatrix} \rho_g \\ \rho_g u_i \\ \rho_g e_o \end{bmatrix}, \qquad \mathbf{F}_j = \begin{bmatrix} \rho_g u_j \\ \rho_g u_i u_j + p\delta_{ij} \\ u_j(\rho_g e_o + p) \end{bmatrix} \tag{2}$$

In this expression, u_i is the fluid velocity component in the i direction, e_o is the specific total energy of the continuous phase, and p is the continuous-phase pressure defined by a typical equation of state. The source terms on the right-hand side of Eq. (1) are due to phase coupling and can be written as

Presented as Paper 2008-793 at the 46th AIAA Aerospace Sciences Meeting and Exhibit, Reno, NV, 7–10 January 2008; received 28 August 2009; revision received 6 May 2010; accepted for publication 7 May 2010.

*Senior Engineer, 601 Oakmont Lane, Suite 220. Student Member AIAA.
†Professor, Aerospace Engineering, 122 Engineer's Way. Associate Fellow AIAA.
‡Senior Engineer, 1525 4th Street. Senior Member AIAA.

$$\mathbf{S} = \begin{bmatrix} -R \\ -D_i \\ -\dot{Q} - \dot{W} - h_f R \end{bmatrix} \tag{3}$$

Here, R is the rate of condensation of the particles per volume of gas, D_i is the drag force of the particles in the i direction per volume of gas, and $\dot{Q}$ is the heat transferred to those particles per volume of gas. The source term for the continuous-phase energy equation per volume of gas includes heat transfer effects ($\dot{Q}$), work done on the particles ($\dot{W}$), and potential energy change associated with the heat of formation of the added mass (h_f). The three terms arise as a result of the three components of total energy: sensible (or thermal) potential energy, kinetic energy, and chemical potential energy.

B. Dispersed-Phase Equations

The Lagrangian dispersed-phase equations for particle diameter d_p, velocity v_i, position x_{pi}, and temperature T_p can be written as (Kersey [10])

$$\frac{\mathrm{d}d_p}{\mathrm{d}t} = -\frac{\rho_g D_v}{2\rho_p d_p} B_p \mathrm{Sh} \tag{4a}$$

$$w_i = v_i - u_i \tag{4b}$$

$$Re_p \equiv \rho_g |\mathbf{w}| d_p / \mu_g \tag{4c}$$

$$\frac{\mathrm{d}v_i}{\mathrm{d}t} = \frac{3}{4}\frac{\rho_g C_D (v_i - u_i)|\mathbf{w}|}{\rho_p d_p} \tag{4d}$$

$$\frac{\mathrm{d}x_{pi}}{\mathrm{d}t} = v_i \tag{4e}$$

$$\frac{\mathrm{d}T_p}{\mathrm{d}t} - \frac{3\lambda_v}{c_s d_p}\frac{\mathrm{d}d_p}{\mathrm{d}t} = \frac{6k_g Nu}{\rho_p c_s d_p^2}(T_g - T_p) \tag{4f}$$

For Eq. (4a), D_v is the diffusion coefficient, B_p is the Spalding transfer number, and Sh is the Sherwood number. This equation is considered reasonable, because the Spalding transfer number was found to be less than 0.02 for the present shock conditions (Kersey [10]). In Eq. (4c), $\mathbf{w}$ is the relative particle velocity vector [defined by Eq. (4b)], which is used to determine the particle Reynolds number Re_p, which in turn is used to obtain the drag coefficient C_D. In Eq. (4f), λ_v is the latent heat of vaporization of the particle, c_s is the particle specific heat, Nu is the Nusselt number, k_g is the thermal conductivity of the continuous phase, and it is assumed that the internal particle temperature is uniform. This is consistent with small drops in weak shock flows [7,9], but is not reasonable for strong shocks, especially if combustion occurs. Note that the gas quantities used for relative velocity and temperature [Eqs. (4b) and (4f)] are hypothetically interpolated to the particle center of mass, neglecting flow interactions with that particular particle.

The Nusselt and Sherwood numbers can be written as functions of particle Reynolds number, Prandtl number, and Schmidt number using the conventional Ranz–Marshall [11] relationships. However, the C_D formulation used in this study includes rarefaction effects (Loth [12]) to account for the small particle sizes. This formulation was shown to compare well with experiments and theoretical limits, including the free-molecular limit of Stadler and Zurick [13] as a function of the Knudsen number:

$$Kn_p = \frac{2\mu_g}{\rho_g d}\sqrt{\frac{\pi}{8\Re_g T_g}} \tag{5}$$

The drag coefficient model and the Ranz–Marshall relationships were found to be appropriate for $Re_p < 50$, which is reasonable for the shock simulations herein with $Re_p < 10$ [10]. For the conditions investigated in this study, blowing effects (drag changes due to evaporation) were found to be negligible because the blowing velocities were very small compared to the relative velocities.

C. Interphase Source Terms to the Gas Phase

The interphase mass transfer term R of Eq. (3) represents the mass rate of vapor condensing on all the particles contained in a unit volume of gas and can be written as

$$R = -\mathrm{Sh}\pi d_p n_p \rho_g D_v B_p \tag{6}$$

The quantity n_p is the particle number density. The inclusion of mass transfer to the interphase physics introduces related terms to the particle governing equations, as previously outlined in Eq. (4).

The interphase momentum coupling term is the force on the dispersed phase from the continuous phase, or simply the drag per unit volume D_i, which can be written as

$$D_i = \pi n_p \rho_g C_D w_i |\mathbf{w}| d_p^2 / 8 \tag{7}$$

The interphase energy coupling term in Eq. (3) includes the work done on the dispersed phase by the continuous phase and the heat transferred from the continuous phase to the dispersed phase:

$$\dot{W} + \dot{Q} = v_i D_i + \dot{Q} = \pi d_p n_p [v_i d_p \rho_g C_D w_i |\mathbf{w}|/8 + Nu(T_g - T_p)k_g] \tag{8}$$

This expression neglects radiation effects, which is reasonable for the present noncombusting conditions.

The chemical potential energy source term to the gas is the rate of mass addition [R from Eq. (6)] multiplied by the heat of formation of the dispersed-phase species (h_f).

D. Particle Response Times

For the discussion of the numerical techniques and the simulations results, it is helpful to identify the mass, momentum and thermal response times of a particle. For mass transfer, consider an isolated droplet in a steady flow at small Re_p conditions so that the right-hand side of Eq. (4a) is constant. Integrating then yields the so-called d^2 law:

$$d_p^2(t) = d_p^2(t_0) - \xi t \tag{9}$$

In this expression, ξ is an evaporation coefficient equal to

$$\xi = 4\rho_g D_v B_p \mathrm{Sh}/\rho_p \tag{10}$$

If this coefficient is constant (reasonable for $Re_p \gg 1$), it allows definition of a droplet lifetime τ_m as

$$\tau_m = d_p^2(t_0)/\xi \tag{11}$$

This is the time it takes for the particle to completely evaporate at a fixed rate.

The Lagrangian dispersed-phase temperature equation (4f) can be rewritten in terms of a thermal response time $\tau_{T,p}$ for the particle or droplet:

$$\frac{\mathrm{d}T_p}{\mathrm{d}t} = \frac{1}{\tau_{T,p}}(T_g - T_p) \tag{12a}$$

$$\tau_{T,p} = \frac{\rho_p c_s d_p^2}{6k_g Nu} \tag{12b}$$

This response time is a measure of the thermal inertia of the particle or how quickly the particle temperature will equilibrate to the surrounding continuous-phase temperature.

Similarly, the momentum response time of the particle or droplet (τ_p) can be defined based on the particle mass, relative velocity, and drag force as

$$\tau_p = \frac{m_p |\mathbf{w}|}{F_D} = \frac{4\rho_p d_p}{3C_D \rho_f |\mathbf{w}|} \tag{13}$$

For the linear drag regime in continuum flow ($Re_p \ll 1$), $C_D = 24/Re_p$ so that the response time becomes proportional to the square

of particle diameter, as also found for thermal response time at small Re_p.

E. Multiphase Numerical Formulation and Particle Ordinary Differential Equation Discretization

The Lagrangian dispersed-phase solver is called before each continuous-phase time step. The Lagrangian formulation tracks trajectories of parcels, where each parcel contains N_{pP} physical particles per parcel that are assumed to all follow the same trajectory (reasonable so long as the parcels are smaller than a computational cell size as stipulated herein). Continuous-phase flow properties at the current time level t^n are linearly interpolated to the particle location to determine the interphase source terms. The new dispersed-phase properties at the next time level (t^{n+1}) are then obtained via the integration schemes discussed below. Within the multiphase solver, calculations are carried out in the order listed in Eq. (4), where the updated particle velocities are used to find the new particle positions. Discretization of these equations is discussed in the following.

For the momentum ordinary differential equation (ODE), the exponential one-step time-integration scheme of Barton [14] is used for the particle velocity and position equations, which assumes a linear drag for each time step:

$$\mathbf{v}^{n+1} = \mathbf{v}^n \exp(-\Delta t/\tau_p^n) + \mathbf{u}^n[1 - \exp(-\Delta t/\tau_p^n)] \tag{14a}$$

$$\mathbf{x}_p^{n+1} = \mathbf{x}_p^n + \tau_p^n(\mathbf{w}^n - \mathbf{g}\tau_p^n)[1 - \exp(-\Delta t/\tau_p^n)] + \mathbf{u}^n \Delta t \tag{14b}$$

This scheme has been found to be accurate to within 1% of the predicted particle velocity for various flows integrated over hundreds of time steps for $Re_p < 65$ (Lee and Loth [15]), which is consistent with the maximum Reynolds number in the present simulations ($Re_p < 50$). However, this level of accuracy requires that the computational time step (Δt) be small compared to both to the particle response time (e.g., $\Delta t < 0.25\tau_p$) and the fluid time scale seen by the particle (e.g., a continuous-phase Courant–Friedrichs–Lewy number of less than 0.5).

To solve the ODEs for particle diameter and temperature, explicit first-order forward-difference schemes are used for the discretized particle diameter and temperature equations:

$$d_p^{n+1} = d_p^n - 2\Delta t \frac{\rho_g D_v}{\rho_p d_p^n} B_p \mathrm{Sh} \tag{15a}$$

$$T_p^{n+1} = T_p^n + \frac{6k_g Nu(T_g^n - T_p^n)\Delta t}{\rho_p c_{p,p}(d_p^n)^2} + \frac{3\lambda_v(d_p^{n+1} - d_p^n)}{c_{p,p} d_p^n} \tag{15b}$$

These simple schemes were found to be reasonably accurate for the present conditions (Kersey et al. [16]).

The continuous-phase solver then solves the Navier–Stokes equations to time level t^{n+1} with cell-averaged interphase source terms identified in Eq. (3). The Eulerian gas flow solver uses a finite volume method in strong conservation form for both structured and unstructured hybrid zonal grids (Bush et al. [17] and Bush [18]). The solution of the Euler equations (including their source terms) is based on a scalar implicit time-stepping method [17]. For cases with shocks, a Roe third-order upwind-biased scheme was used with a Koren total-variation-diminishing limiter (Koren [19]). The net interphase mass and force transfer terms are based on a summation over all parcels in the cell (where P is the total number of parcels in a cell and each parcel k contains $N_{\mathrm{pP},k}$ particles):

$$\forall_{\mathrm{cell}} R = -\sum_{k=1}^{P} N_{\mathrm{pP},k} \mathrm{Sh} \pi d_{p,k} \rho_g D_v B_{p,k} \tag{16a}$$

$$\forall_{\mathrm{cell}} D_i = \frac{\pi}{8} \sum_{k=1}^{P} N_{\mathrm{pP},k} \rho_g C_{D,k} w_{i,k} |\mathbf{w}_{i,k}| d_{p,k}^2 \tag{16b}$$

This method was found to be accurate (to within 1%) and stable for the noncombusting flows considered herein and avoids the need for intermediate quantities (as used by Amsden et al. [20]), which improves overall efficiency and programming modularity. The present coupling scheme requires eight or more parcels per Eulerian computational cell for accuracy (consistent with results of Sivier et al. [7]). The grid and time-step resolution requirements in the context of the shock attenuation cases are discussed in Sec. I.

F. Verification of Thermal and Energy Coupling to the Dispersed Phase

For constant gas-phase temperatures and a constant thermal response time, an analytical solution for the particle temperature can be obtained by integrating Eq. (12):

$$T_p(t) = T_p(t_0) \cdot \exp(-t/\tau_{T,p}) + T_g[1 - \exp(-t/\tau_{T,p})] \tag{17}$$

One-way heat transfer to a solid dispersed phase was tested using a simple steady flow problem in a 1-m-long straight duct and compared to the above analytical solution. The gas temperature was kept constant at 300 K and the particle relative velocity was set to zero so that the Nusselt number was equal to 2.0. The thermal response time was chosen to be approximately 0.60 s. The initial particle temperature was 400 K. As shown in Fig. 1, the convective heat transfer to the dispersed phase in the current formulation shows excellent agreement with the analytical solution, indicating reasonable accuracy of the numerical scheme.

For verification of two-way energy coupling, an analytical solution was derived for the continuous-phase temperature increase due to work done by the particles. The gas temperature was set to 300 K at the inflow of a 1-m-long straight duct. The gas-phase velocity was set at 5 m/s, a small value compared to the speed of sound, such that

$$e_o = e + \tfrac{1}{2}u^2 \approx e \tag{18}$$

Heat transfer between phases was disabled such that the interphase heat transfer term $\dot{Q}$ was zero. Further assuming large relative velocities compared to the gas-phase velocity ($v \gg u$) such that $v \approx w$, the Lagrangian form of the gas energy-conservation equation can be reduced to

$$\frac{\mathrm{d}T_g}{\mathrm{d}t} = v \frac{\pi}{8} \frac{n_p C_D w_i |\mathbf{w}| d_p^2}{c_{p,g}} \tag{19}$$

The particle velocity was held artificially constant (in this case, 100 m/s), so this can be integrated to give

$$T_g(t) = T_g(t_0) + v \frac{\pi}{8} \frac{n_p}{c_{p,g}} C_D w_i |\mathbf{w}| d_p^2 t \tag{20}$$

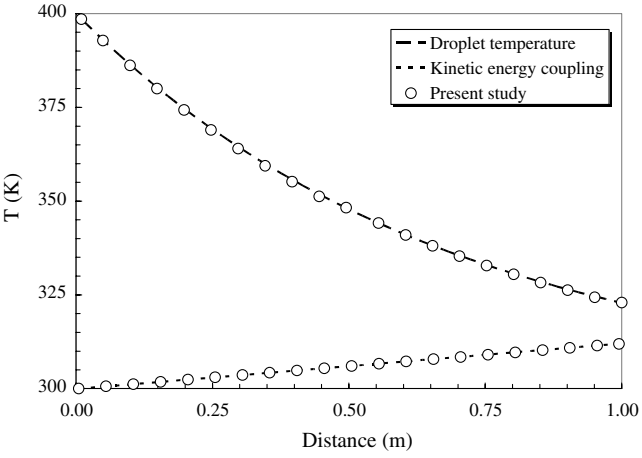

Fig. 1 Comparison of interphase heat transfer in a straight duct for two different cases (shown in one plot): one-way coupling to verify droplet temperature change (where T refers to T_p) and kinetic energy coupling to verify gas-temperature change (where T refers to T_g). Lines are analytical solutions and symbols are numerical solutions.

Assuming steady gas-phase velocity, the temperature distribution is given by

$$T_g(x) = T_g(x_0) + v\frac{\pi}{8}\frac{n_p}{c_{p,g}}C_D w_i |\mathbf{w}| d_p^2 x \tag{21}$$

For the simulations, particle mass transfer was set to zero, a particle diameter of 300 μm was chosen (and the corresponding drag coefficient was assumed to be constant at 0.424), and the gas phase was taken as air at standard conditions. The particle number density n_p was chosen to be 17,250 particles/m^3 to give a theoretical temperature change of approximately 12 K over a 1 m distance. The results from the current formulation are also compared to this analytical solution in Fig. 1. As shown, the current implementation accurately predicts the interphase kinetic energy coupling effects. A similar verification was conducted for one-way convective heat transfer from the dispersed phase to the continuous phase Additionally, transient droplet temperatures were simulated with finite Reynolds number conditions for warm water droplets injected into a colder dry gas and showed excellent agreement with previous simulations (Kersey et al. [16]).

G. Verification of Interphase Mass and Momentum Transfer to Drops for Low-Speed Flow

To verify the present methodology for droplet evaporation and velocity response at low speeds, simulations of a one-dimensional flow were conducted to model water sprays in wind tunnels. A low-speed formulation based on Willbanks and Schulz [21] (hereafter referred to as Schulz–Willbanks) was compared to the present technique for the uniform injection of water droplets in air in a straight duct 20 ft long with a 36 ft^2 square cross section. Consistent with Schulz–Willbanks, a uniform gas velocity of 220 ft/s and temperature of 492°R was specified, along with an initial vapor mass fraction of water of 3.175×10^{-3}. For the droplets, the initial liquid water content (LWC) was prescribed as 1.0 g/m^3 for three droplet diameters, 25, 100, and 1000 μm. Initial drop temperature was set at 600°R and an initial drop velocity of 100 ft/s was set to generate a high degree of nonequilibrium. There are some minor differences between the two codes in terms of the equations and the numerics. For example, Schulz–Willbanks uses a single third-order polynomial fit for latent heat of vaporization and a seven coefficient exponential fit for vapor pressure. In comparison, the present method uses linear interpolation between values in lookup tables with intervals of 10 K for vapor pressure and 100 K for latent heat. There are some other small differences with respect to the drag coefficient expression and heat transfer formulation for the present flow conditions.

The change in droplet diameter as a function of axial distance is plotted in Fig. 2a and shows good agreement between the present formulation and Schulz–Willbanks. The final diameter of the 100 and 1000 μm droplet cases predicted by the present method are within 1% of that for Schulz–Willbanks. Relative velocity is plotted for all three cases in Fig. 2b. There is again good agreement across all drop diameters. The largest disparity in relative velocities occurs in the 1000 μm case, which is less than 2% at the final downstream station and can be attributed to differences noted above. However, it is noteworthy that the Schulz–Willbanks code exhibited minor numerical oscillations for some conditions, while the present formulation was free of such behavior.

H. Verification of Two-Way Coupling for Dusty Shocks with Very Small Particles

In the limit of very small particles, the two-way coupling effects associated with the effective density can be described analytically with a mixed-fluid approximation that assumes the dispersed-phase and the continuous phase are in local kinetic and thermal equilibrium: $u_m = v = u$ and $T_m = T_p = T_g$. The mixed-fluid approach is reasonable when the particle momentum and thermal response times are small compared to the time scales of the fluid velocity and temperature changes.

The corresponding mixture thermal properties vary only with particle loading. In the limit of very high density particles ($\rho_p \gg \rho_g$)

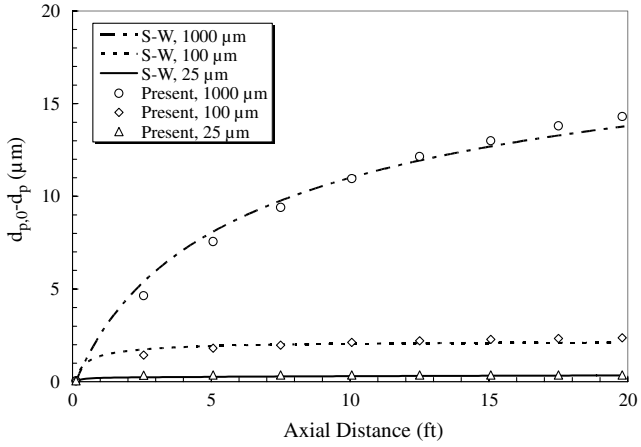

a)

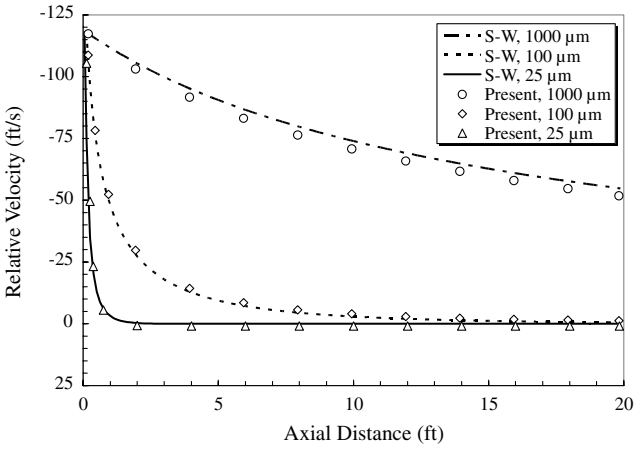

b)

Fig. 2 Simulations and theory of water droplets with an initial temperature of 600°R injected at an initial velocity of 100 ft/s into a straight duct of dry air at 492°R moving at 220 ft/s: a) droplet diameter change and b) relative velocity.

and very small volume fraction of the particle per unit volume of mixture, the mixture density expression can be approximated in terms of the particle loading factor η as

$$\rho_m \approx \rho_g(1+\eta) \tag{22}$$

The mixed-fluid approximation results in a single set of conservation equations for the flow mixture. Assuming that the mixed fluid obeys an ideal equation of state, the mixed-fluid pressure ($p_m = p_g$), gas constant $\Re_m$, specific heat $c_{p,m}$. and specific heat ratio γ_m can be defined, respectively, as

$$p_m = \rho_m \Re_m T_m \tag{23a}$$

$$\Re_m = \Re_g/(1+\eta) \tag{23b}$$

$$c_{p,m} \approx (c_{p,g} + \eta c_s)/(1+\eta) \tag{23c}$$

$$\gamma_m \equiv \frac{c_{p,m}}{c_{\forall,m}} = \frac{c_{p,g}+c_s\eta}{c_{\forall,g}+c_s\eta} = \gamma_g\left(\frac{c_{p,g}+c_s\eta}{c_{p,g}+\gamma_g c_s\eta}\right) \tag{23d}$$

where c_s is the specific heat of the particles, $c_{p,g}$ is the specific heat of the gas at constant pressure, and $c_{\forall,g}$ is the specific heat of the gas at constant volume. From the mixed-fluid specific heat ratio and gas constant, the acoustic speed can be obtained as

$$\frac{a_m^2}{a_g^2} = \frac{\gamma_m \Re_m}{\gamma_g \Re_g} = \frac{1 + c_s^* \eta}{(1+\eta)(1+\gamma_g c_s^* \eta)} \tag{24}$$

where the normalized specific heat between the particles and the gas is given as $c_s^* \equiv c_s / c_{p,g}$. Often this ratio is taken as unity for the dusty-gas limit to simplify the analytical solution (Miura and Glass [22]) but is herein considered as a variable.

For a normal shock propagating into quiescent gas, a shock Mach number can be defined as

$$M_{\text{sh}} \equiv V_{\text{sh}} / a_1 \tag{25}$$

where V_{sh} is the speed of the shock relative to a fixed frame and a_1 is the speed of sound in the unshocked medium. Standard shock relations can then be used to define the changes across the wave (Kersey et al. [16]). In the case of a shock wave propagating from air into a dusty-gas mixture of glass particles, the shock wave S_o will be refracted at the interface and a reflected shock will form. A contact discontinuity C forms in the region between the reflected S_R and transmitted S shocks at the interface between the clean air and the dusty gas. This is shown schematically in Fig. 3 and the various regions are labeled for reference. The gas velocity behind the reflected shock can be written as (Sommerfeld [4])

$$\frac{u_{m3}}{a_1} = \frac{u_{m2}}{a_1} - \frac{a_2}{a_1}\sqrt{\frac{2}{\gamma(\gamma+1)}\left(\frac{p_{m3}}{p_{m2}} - 1\right)\left(\frac{p_{m3}}{p_{m2}} - \frac{\gamma-1}{\gamma+1}\right)^{-1/2}} \tag{26}$$

The velocity of the mixed fluid behind the transmitted shock can then be written as

$$\frac{u_{m2'}}{a_1} = \frac{a_m}{a_1}\sqrt{\frac{2}{\gamma_m(\gamma_m+1)}\left(\frac{p_{m2'}}{p_{m1}} - 1\right)\left(\frac{p_{m2'}}{p_{m1}} - \frac{\gamma_m-1}{\gamma_m+1}\right)^{-1/2}} \tag{27}$$

Furthermore, across the contact discontinuity $p_{m3} = p_{m2'}$ and $u_{m3} = u_{m2'}$.

Solving Eqs. (26) and (27) yields the pressure ratios across the reflected and transmitted shocks. The Mach number of the transmitted shock wave can then be calculated as

$$M'_{\text{sh},m} = \sqrt{\left(\frac{p_{2'}}{p_1} - 1\right)\frac{\gamma_m + 1}{2\gamma_m} + 1} \tag{28a}$$

$$M_{\text{sh},m} = M'_{\text{sh},m}(a_m / a_1) \tag{28b}$$

Using these relations, consider a dusty-gas mixture of air (at standard conditions) and glass particles with a density ρ_p of 2500 kg/m^3 and a specific heat $c_{p,p}$ of 766 J/(kg-K) at a mass loading η of 0.63 the effective density ρ_m is 1.96 kg/m^3. For a shock propagating into this dusty-gas mixture at a Mach number of 1.49, the equilibrium shock Mach number is 1.146. To examine this theoretical limit numerically, 1-μm-diam particles were considered with the above conditions. Figure 4 compares the shock attenuation results from the present method to the theoretical result for an infinitely small particle. The simulated shock attenuates to an equilibrium shock Mach number that agrees well with the theoretical equilibrium.

I. Validation of Solid-Particle Shock Attenuation for Particles with Finite Response Time

The current numerical method was next used to study shock attenuation by solid particles. For this, a normal shock was initialized in pure air in a shock tube following Sivier et al. [7]. The shock was located 10 cm upstream of a dusty-gas mixture of 27-μm-diam spherical glass particles with a density (ρ_p) of 2.5 g/cm^3 and a specific heat ($c_{p,p}$) of 766 J/(kg-K). Several structured grids were tested to test grid refinement with x spacing ranging from 0.25 cm to 1 cm and y and z spacing held constant at 1 cm because of the one-dimensional nature of the flow. To test temporal discretization, time steps were varied from 2×10^{-7} s to 2.5×10^{-6} s with these grid configurations. Based on these studies, spatial and temporal independence was reasonably achieved (based on 1% accuracy of the propagating shock speed) with a 0.5 cm spacing in the x direction and a time step of 4×10^{-7} s for both nonevaporating and evaporating conditions. While the distance for the shock to reach equilibrium can vary significantly based on conditions, the required spatial resolution generally corresponded to less than 1% of the distance required for the shock to reach equilibrium. The required time step corresponded to less than 5% of the particle response time (and less than 0.02% of the time required for the shock to reach equilibrium conditions).

Shock Mach number as a function of position was then calculated and compared to experimental and numerical data from Sommerfeld [4], Sivier et al. [7], and recent numerical results from Haselbacher et al. [8]. Figure 5a shows the shock attenuation for an initial shock Mach number $M_{s,0}$ of 1.49 and a particle loading (η) of 0.63. Measurements of shock position are relative to the initial particle interface. While there is reasonable agreement with previous experimental and numerical data in the first half-meter of the domain, the current method predicts stronger shock attenuation. The final shock Mach number predicted is 1.167: 2.6% lower than that predicted by previous studies. Shock attenuation for the same initial shock Mach number of 1.49 and a higher loading of 1.25 is shown in Fig. 5b. Here, the present method yields good agreement with the experimental data and numerical data. A case with a different Mach number was also simulated and compared to both experiments and numerical results and yielded similar results (Kersey et al. [16]). The present method predicts a final shock Mack number <1% lower than Sommerfeld's method and 2% lower than Sivier et al.'s [7] method. These small variations may be attributed to minor differences in the

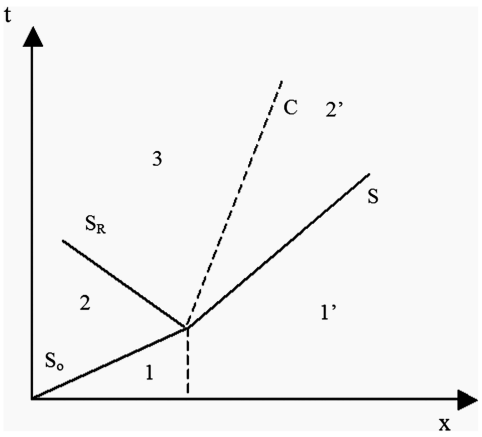

Fig. 3 Gas-dynamic interaction of a shock wave propagating from clean air (1) into a dusty gas (1′), where *C* indicates the contact discontinuity and *S* indicates a shock path.

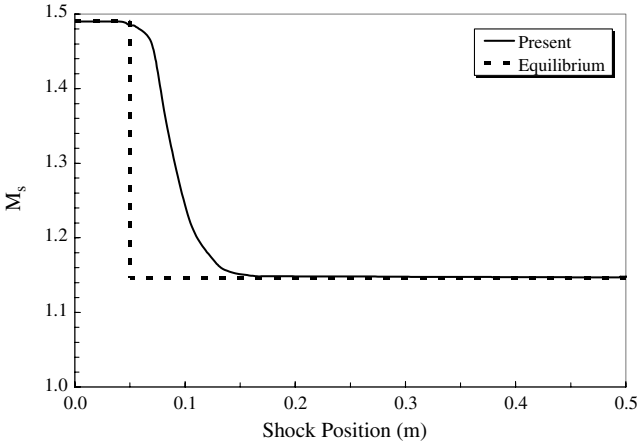

Fig. 4 Shock position vs shock Mach number for $M_{s,0} = 1.49$ and $\eta = 0.63$ comparing present simulation with 1 μm particles with equilibrium theory for infinitely small particles.

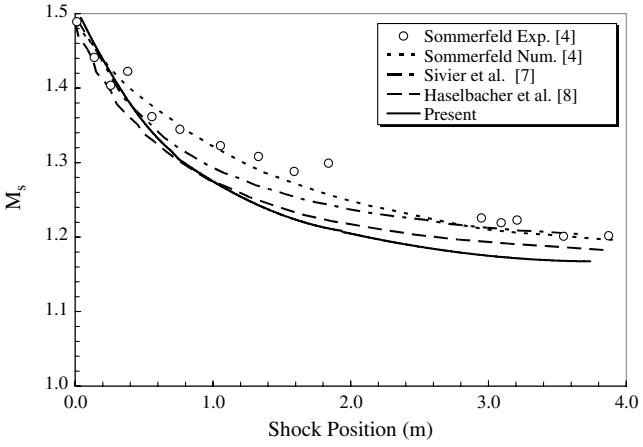

a)

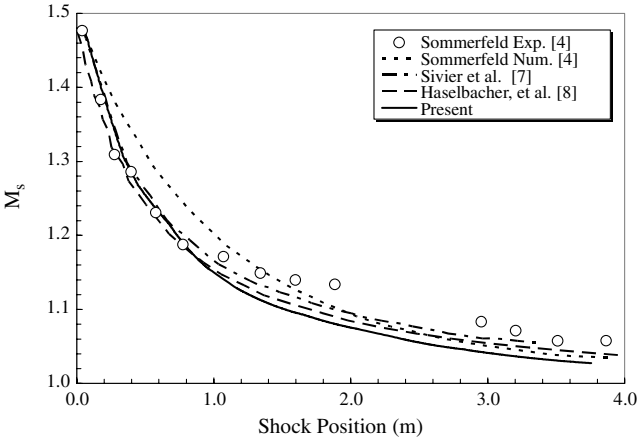

b)

Fig. 5 Plots of a) evolution of shock strength as a function of position for $M_{s,0} = 1.49$ and $\eta = 0.63$ and b) evolution of shock strength as a function of position for $M_{s,0} = 1.49$ and $\eta = 1.25$.

numerical schemes for shock-capturing, since use of different drag coefficient formulations were found to have little effect on the present simulations.

It is interesting that beyond 1 m, all numerical predictions show faster attenuation than the measured experimental data. The reason for this difference is not clear, but may be due to preferential concentration of the particles (pockets of flow where particle concentrations are higher). Such conditions can arise when small particles are suspended and dispersed by turbulence (Eaton and Fessler [23]) as is the case just before the shock propagation. Even if no coalescence occurs, this effect increases relative particle velocity and drag for a given gravitational force (Aliseda et al. [24]), which thus reduces the shock attenuation, qualitatively consistent with the numerical underprediction of shock Mach number. If particle collisions cause coalescence or clumping, this will increase the effective particle size, which increases the time and distance needed to reach equilibrium.

III. Results of Shock Attenuation by Evaporating Drops

A. Coupling Physics and Test Matrix

The validated numerical methodology was used to perform a parametric study on shock attenuation by liquid water droplets. As stated in the introduction, the most relevant previous numerical work found by the author was that by Chang and Kailasanath [9]. However, their study did not examine effects of evaporation rate or particle inertia on shock attenuation and did not investigate effects of mass loading or particle size. Another study performed by Goossens et al. [3] used experimental and theoretical techniques to examine the effect of shock waves on evaporation for relatively small droplets (approximately a few microns) so that breakup could be neglected. However, this study did not include numerical predictions, did not investigate the effects of evaporation on shock decay, and was limited to low mass loading cases (0.4–0.6%) with one-way coupling to only the particle phase. Herein, we hope to use the present numerical method to understand how relatively small evaporating drops (which do not breakup) affect the shock attenuation and to investigate the interaction physics under a wide range of particle conditions.

For the gas, the preshocked temperature and pressure were taken to be 275 K and 0.66 bar, respectively, consistent with the study by Goossens et al. [3] To avoid the complex physics and empiricism of a droplet breakup model, the present test conditions were chosen such that the droplet Weber number would be less than 8 throughout the simulation, making droplet breakup effects unlikely. As such, the maximum droplet diameter was limited to 20 μm for an initial shock Mach number of 1.25 and to 2.4 μm for an initial shock Mach number of 1.5 (Table 1). This set of conditions may be reasonable for high-pressure spray systems in flows with moderate Mach numbers. The duct geometry, grid, and numerical methods were the same as those used in the solid-particle shock attenuation study above. Initial water vapor mass fraction was set to 0.00646 to achieve 100% humidity in the preshock (quiescent) region, thereby limiting evaporation (or condensation) to the postshock region. A multispecies model was used for the continuous phase to solve the transport of the three species equations for H_2O (vapor), N_2, and O_2. This is somewhat different from the Goossens et al. study, which considered humid nitrogen (i.e., no O_2).

The test matrix was developed to examine the effects of Mach number, mass loading, drop size, specific heat ratio (c_s^*), and evaporation on shock attenuation with five sets of runs, each to study a specific effect (Table 1). Case study 1 included two Mach numbers, 1.25 and 1.5, to determine Mach number effects and to compare evaporation rate to data taken by Goossens et al. [3]. Case study 2 includes several mass loadings ranging from 0.005 to 5.0 to determine the effect of particle concentration. Case study 3 includes a range of droplet diameters from 2.4 to 20 μm (limited by Weber number constraints) to study how drop size affects shock attenuation. Case study 4 examined two specific heat ratios c_s^*: 4.17, consistent with liquid water in air, and 1.0, consistent with previous analytical studies (Miura and Glass [22]) and closer to that of liquid fuel in a fuel–air mixture. Case study 5 examined these same two specific heats ratios but without any evaporation effects.

The baseline condition first investigated is that given by case study 1 for an initial shock Mach number of 1.25 and a very low mass loading of 0.5%. Gas, particle, and relative velocity are shown in Fig. 6a as a function of position at $t = 2.4$ ms, which is the time at which the shock would have traveled 1 m in pure gas. Because of the low mass loading, there is negligible shock attenuation and the shock

Table 1 Test matrix for liquid-droplet shock attenuation

Case study	Mach no.	Diam, μm	Mass loading	Specific heat ratio	Evaporation?
1	1.25, 1.5	2.4	0.005	4.17	Yes
2	1.25	2.4	0.02, 0.1, 0.63, 5.0	4.17	Yes
3	1.25	2.4, 5.0, 20	0.63	4.17	Yes
4	1.25	2.4	0.63	1.0, 4.17	Yes
5	1.25	2.4	0.63	1.0, 4.17	No

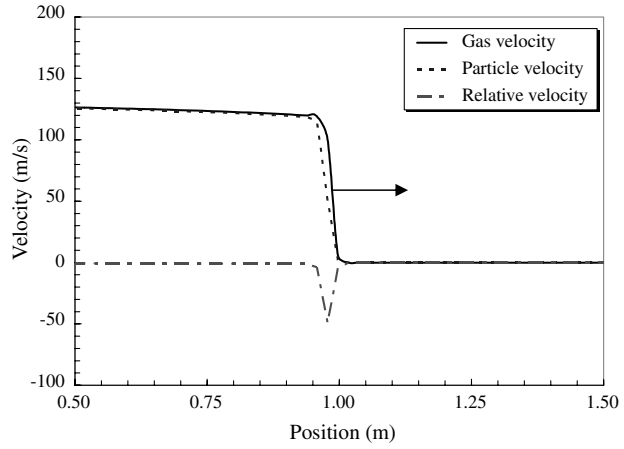

a)

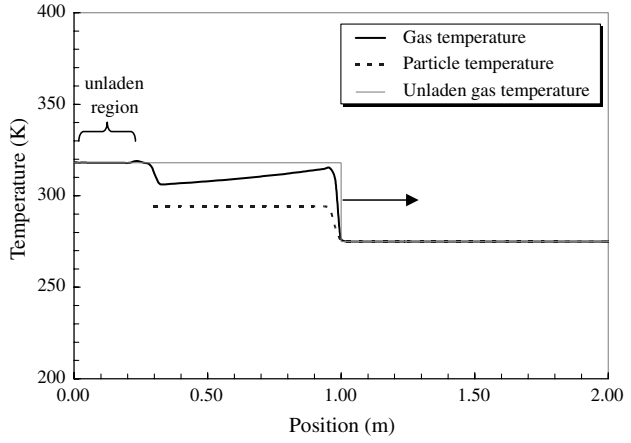

b)

Fig. 6 Plots of a) instantaneous gas, particle, and relative velocity through the shock front for an initial shock Mach number of 1.25 and a loading of 0.5% for case study 1, where the shock is moving to the right (indicated by the arrow) and induces a positive velocity behind it, and b) instantaneous gas and particle temperature as a function of position for an initial shock Mach number of 1.25 and a loading of 0.5% with unladen value for comparison for case study 1.

front has propagated essentially as far as an unladen shock: i.e., the front is centered nearly at $x = 1$ m. The drop velocity quickly equilibrates to the postshock gas velocity due to the small particle response time.

Gas and particle temperatures for these conditions are shown in Fig. 6b, along with the theoretical unladen gas temperature. Immediately behind the shock, the gas temperature rises toward the postshock value. However, unlike particle velocity, particle temperature does not equilibrate to the surrounding gas. Instead, the droplet temperatures rise quickly behind the shock until wet-bulb temperature (294 K for these conditions) is reached, which corresponds to a thermal balance between the heat transferred to the drops from the gas phase and the energy required for evaporation. As such, a quasi-steady state is reached where drop temperature is constant and only evaporation occurs. However, because the interphase heat transfer to the continuous phase is based on the temperature difference between the continuous and dispersed phases [Eqs. (3) and (8)], the gas temperature then decreases in near-linear fashion from $x = 0.95$ to 0.3 m. The decrease is significant (more than 10 K) despite a mass loading too small to effect shocks in the case of solid (nonevaporating) particles. At $x = 0.3$ m, there is a particle loading discontinuity between the gas-particle mixture ($x > 0.3$ m) and the unladen (single-phase) gas ($x < 0.3$ m), where the temperature rises, consistent with the unladen shock relationships

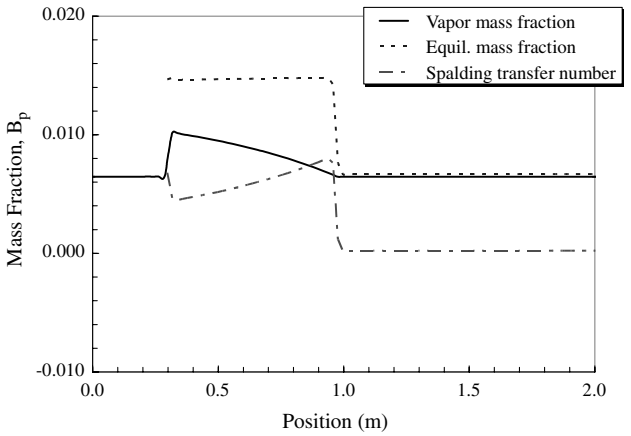

Fig. 7 Instantaneous vapor mass fraction, equilibrium mass fraction at the droplet surface, and Spalding transfer number for $M_{s,0} = 1.25$ and a loading of 0.5% for case study 1.

Figure 7 shows water vapor mass fraction in the gas, equilibrium vapor mass fraction at the droplet surface, and the Spalding transfer number. Equilibrium (saturation) vapor mass fraction at the droplet surface increases quickly behind the shock, because it is solely a function of droplet surface temperature. Between $x = 0.3$ and 0.95 m, the equilibrium mass fraction is a constant 0.015, corresponding to the droplet wet-bulb temperature (294 K). The actual mass fraction of vapor in the gas is saturated before the shock hits, but just behind the shock the mass fraction is less than the saturated value due to the increase in gas temperature, thus causing evaporation (indicated by the positive Spalding number). This vapor mass fraction then has an approximately linear increase due to the evaporating droplets until the loading discontinuity. Beyond this point ($x < 0.3$ m), the mass fraction of vapor in the gas returns to the specified preshock value (0.00646). Note that the loading discontinuity ($x \sim 0.3$ m) is diffused over two–three times as many cells as the shock front ($x \sim 1.0$ m), and the former is attributed to the interpolation from the Eulerian continuous phase to the Lagrangian dispersed phase and the associated distribution of interphase source terms to surrounding Eulerian nodes.

B. Mach Number Effects

An additional shock Mach number of 1.5 was tested with all other conditions the same as in Sec. III.A to examine Mach number effects. Gas temperatures for the two shock Mach numbers are plotted in Fig. 8a, along with the respective unladen gas-temperature values for an initial particle mass loading of 0.5%. Despite this low mass loading, significant two-way coupling effect on gas temperature due to evaporation (on the order of 5% decrease) is observed. In general, the gas temperature initially increases behind the shock but then decays as heat is transferred to the dispersed phase, especially for the higher shock Mach number. The extent of the droplet presence at this time is shown by vertical arrows and indicates that the Mach 1.5 case includes a region roughly between $x = 0.5$ and 0.62 m for which all the droplets have evaporated. In this region, the gas temperature is constant (since there is no more interphase mass or heat transfer), while the region closer to the shock that contains liquid drops shows a gas-temperature decrease for positions further away from the shock. The interface separating these two regions constitutes a contact discontinuity not seen in the Mach 1.25 case at this instance (though it will develop at a later time for this case).

The relative humidity for both shock Mach numbers is plotted in Fig. 8b. Preshock, the relative humidity for both cases is 100% and there is no evaporation. Postshock, the higher gas-temperatures result in a higher equilibrium mass fraction (Fig. 7) so that the relative humidity is reduced. Since the lower shock Mach number results in a lower gas temperature, this results in a higher relative humidity postshock as compared to the higher shock Mach number. Additionally, for $M_{s,0} = 1.25$, the relative humidity increases linearly as drops evaporate, up until the contact discontinuity at

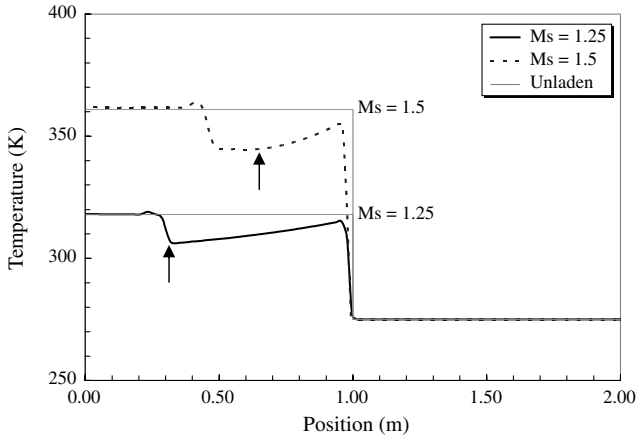

a)

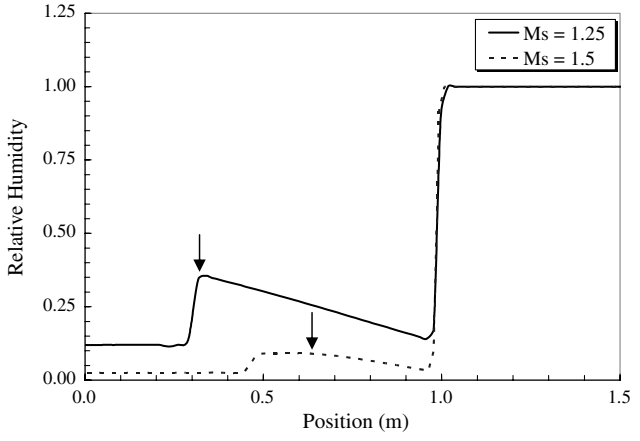

b)

Fig. 8 Plots of a) instantaneous gas-temperature comparison for $M_{s,0} = 1.25, 1.5$ for a loading of 0.5% for case study 1, where vertical arrows indicate the leftward extent of liquid droplets, and b) instantaneous relative humidity comparison for $M_{s,0} = 1.25, 1.5$ and a loading of 0.5% for case study 1, where vertical arrows indicate the leftward extent of liquid droplets.

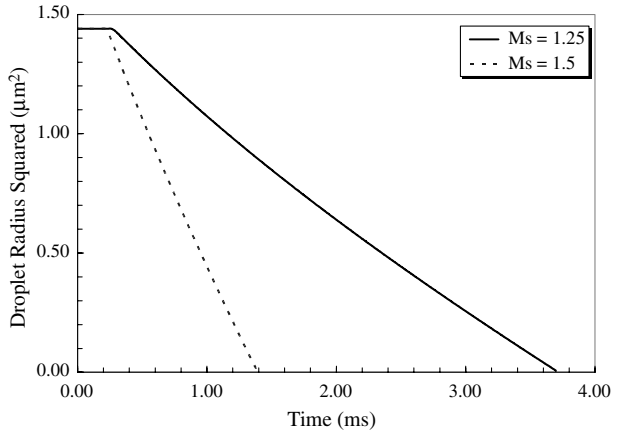

a)

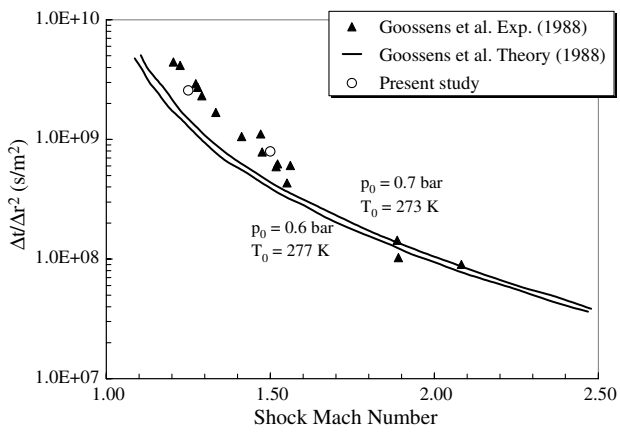

b)

Fig. 9 Plots of a) evolution of droplet radius as a function of time for $M_{s,0} = 1.25$ and 1.5 at a loading of 0.5% for case study 1 and b) evaporation time for drops as a function of initial shock strength with comparison to data from Goossens et al. [3].

$x = 0.3$ m. Beyond this, the relative humidity is reduced to the unladen value corresponding to the specified vapor mass fraction for the unladen gas. For the higher shock Mach number, the relative humidity increases linearly between $x = 0.95$ and 0.62 m, but then remains constant until $x = 0.5$ m due to higher gas temperatures for this region (Fig. 8a). For both Mach numbers, the relative humidity then reduces to the unladen value far downstream (to the left) of the shock.

Evaporation effects are shown in Fig. 9a by plotting the square of the droplet radius as a function of time since passing through the shock wave. Initially, there is little change in droplet radius, an effect noticed by Goossens et al. [3] in their experiments, which they attributed to the rapid buildup in vapor pressure by shock compression, while the droplet temperatures are still close to the initial preshock value. Further behind the shocks, the slope is nearly linear, indicating that the evaporation approximately follows the d^2 law of evaporation from Eq. (9). This is somewhat surprising, since the d^2 law assumes small Reynolds number, but Re_p values as large as 49 were noted just behind the shock for the largest drop and strongest shock (Kersey et al. [16]). The approximate d^2 dependence suggests that droplet lifetimes can be approximately predicted with analytical models assuming a nearly constant evaporation coefficient if the temperature and humidity differences can be appropriately estimated. The is demonstrated in Fig. 9b, which shows the evaporation times predicted by the present study for shock Mach numbers of 1.25 and 1.5 compared to experimental data obtained by Goossens et al. [3] and their theoretical model, which assumes a constant evaporation coefficient. As shown, there is excellent agreement between the present study (which allows for nonlinear effects) and the experimental data. The linearized theory is qualitatively consistent with the experiments and the simulations but tends to underpredict the time required for evaporation. Goossens et al. attributed this to their theoretical assumptions, which assumes linear drag and heat transfer and neglects two-way coupling effects. As shown in Fig. 8a, even very low loadings can cause significant heat loss in the gas behind the shock consistent with an overprediction of postshock gas temperatures for a one-way coupling assumption and an underprediction of evaporation time as in Fig. 9b.

C. Mass Loading Effects

Because the mass loading was shown to be an important consideration, a range of mass loadings was investigated from 0.005 to 5.0, where again the initial shock Mach number was 1.25 and the drop diameter was 2.4 μm. Mixed-fluid theory for solid particles suggests that as the mass loading increases, the equilibrium shock Mach number should decrease. This is also consistent for evaporating cases as shown by the shock attenuation results of Fig. 10a. For mass loadings of 0.63 and 5.0, the theoretical equilibrium shock Mach numbers from mixed fluid theory (0.89 and 0.48, respectively) are shown in the figure, demonstrating excellent comparison to the predicted values. Additionally, it can be seen that for a given diameter, increased mass loading increases the rate of shock attenuation; i.e., the distance required to reach this equilibrium is reduced. This nonequilibrium effect has not previously been

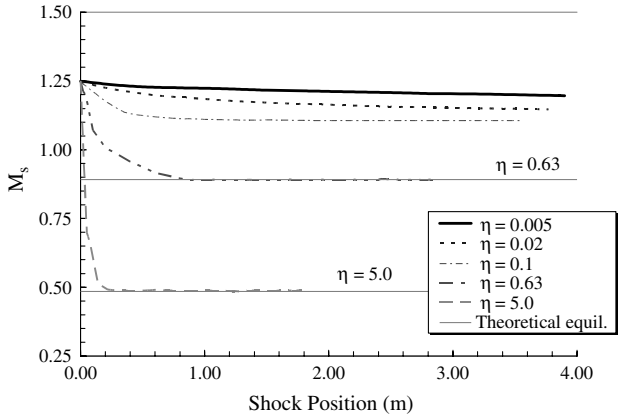

a)

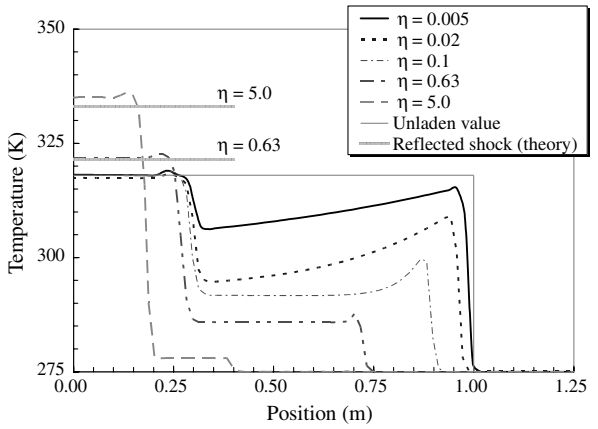

b)

Fig. 10 Plots of a) evolution of shock strength as a function of position for an initial shock Mach number of 1.25 for case study 2 (theoretical equilibrium shock Mach numbers from mixed-fluid theory are included for the two high-mass-loading cases) and b) instantaneous gas-temperature comparison for a range of mass loadings for $M_{s,0} = 1.25$ for case study 2 (mixed-fluid theoretical values for gas temperature behind the reflected shock are also shown for the two high-mass-loading cases).

reported but can be explained qualitatively by considering the change in the *gas* Lagrangian temperature equation due to only heat transfer effects from the droplets:

$$\frac{dT_g}{dt} = \frac{1}{\tau_{T,g}}(T_p - T_g) \tag{29a}$$

$$\tau_{T,g} \equiv \frac{\rho_g c_{p,g}}{\pi N u k_g n_p d_p} \tag{29b}$$

This equation stems from Eqs. (1–3) but is written in a form similar to that used for the particles [Eq. (12)]. In this expression $\tau_{T,g}$ is defined as a gas-phase thermal time scale that reduces as particle concentration increases. Thus, an increased mass loading should result in faster continuous-phase transients and a shorter shock travel distance to reach equilibrium conditions.

Gas temperature is plotted in Fig. 10b for the five different mass loadings studied with comparison to an unladen shock. As loading increases, more heat is consumed in evaporating drops, resulting in lower gas temperatures in the drop-laden region just behind the shock. Increases in loading also cause a reflected shock to be sent upstream (S_R in Fig. 3), which causes a rise in gas temperature far behind the shock (e.g., $x < 0.2$ m) yielding values higher than the unladen value (Sommerfeld [4]). For the highest loadings of 0.63 and 5.0, the gas temperatures far behind the reflected shock, calculated from mixed-fluid theory, are 321 and 333 K, respectively, and are also plotted in Fig. 10b for comparison. For a loading of 0.63, there is excellent agreement between the present study and mixed-fluid theory for $x < 0.2$ m. At the higher loading of 5.0, however, the present study predicts a temperature far behind the reflected shock, which is 2 K greater than the mixed-fluid theory, which may be attributed to the finite mass transfer and inertia effects. Note that if the gas temperature is considered at earlier times (not shown), this reflected shock has not reached the $x = 0$ position yet such that the predicted gas temperature at this point is equal to the unladen postshock value of 317 K.

Figure 11a shows relative temperature ($T_p - T_g$) as a function of position for each mass loading. For the smallest mass loading of 0.005, the rapid increase in gas temperature at the shock front yields a rapid spike in relative temperature. Further away from the shock, none of the droplets have completely evaporated yet so that the relative temperature decreases but remains finite and negative (indicating that the droplets are still not as hot as the surrounding gas). As the mass loading increases and the shock is attenuated more, the initial spike in gas temperature behind the shock is reduced (at a given instant in time due to shock attenuation) so that the relative temperature is also reduced (to less than 1 K at the highest mass loading.

Relative humidity, plotted in Fig. 11b for each mass loading, demonstrates the complex interaction between the evaporating drops and the gas behind the shock wave. In front of the shock wave, the relative humidity for all cases is 100%, as specified. Immediately behind the shock, as gas temperature rises, the relative humidity decreases. Evaporation behind the shock causes relative humidity to then increase. At higher mass loadings, the increased thermal coupling of the drops reduces gas temperature such that the relative

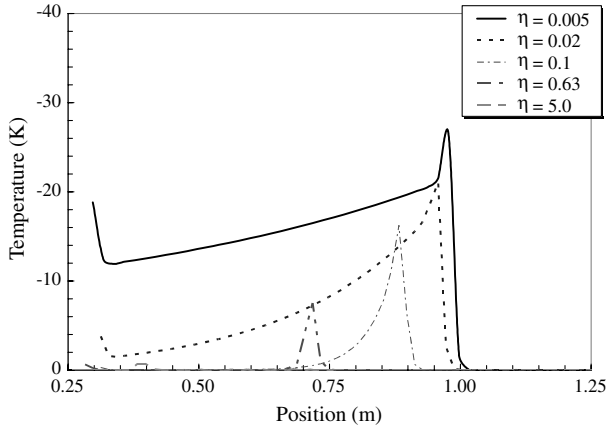

a)

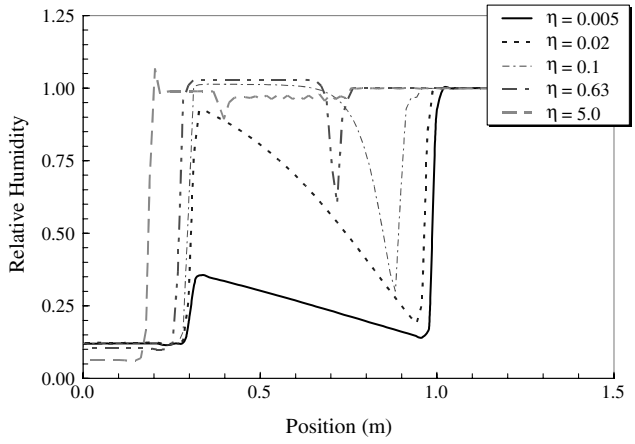

b)

Fig. 11 Plots with a range of mass loadings for $M_{s,0} = 1.25$ for case study 2 for comparison with a) instantaneous relative temperature and b) instantaneous relative humidity comparison.

Table 2 Particle Knudsen numbers pre- and postshock

Kn_p	$d = 0.1$ μm	$d = 0.5$ μm	$d = 2.4$ μm	$d = 5.0$ μm	$d = 20$ μm
Preshock	—	—	0.039	0.019	0.005
Postshock	0.678	0.136	0.028	0.014	0.003

humidity can approach 100%. This can be seen in Fig. 11b for a loading of 0.1 where relative humidity reaches 100% and is then constant until the contact discontinuity between the unladen postshock gas and the gas-particle mixture. At this point, the system comes to equilibrium and evaporation stops (which is also consistent with a negligible difference in relative temperature shown in Fig. 11a at high mass loading). Thus, mass loadings of 0.1 or more include a postshock region where evaporation ceases and thermal equilibrium is reached. For a loading of 0.63 the relative humidity even becomes slightly greater than 100%, indicating supersaturation, but at a mass loading of 5.0, there is evidence of numerical instabilities. As such, implicit schemes (as used in reacting flows) for the vapor species as well as droplet temperature and radius may be helpful when simulating such high loadings.

D. Droplet Size Effects

While it is well known that an increase in particle response time (due to larger particle diameter) increases the distance needed to reach the equilibrium shock Mach number (Chang and Kailasanath [9]), the behavior with evaporating drops is not as well understood. Herein, three initial droplet diameters (2.4, 5, and 20 μm) were tested with a mass loading η of 0.63 and an initial shock Mach number of 1.25. The results for evaporating drops are shown in Fig. 12a (with comparison to the mixed-fluid theoretical value of 0.89) where it can be observed that there is a qualitatively similar increase in distance required for equilibrium conditions as drop diameter increases. In fact, the largest drop size (20 μm) does not fully attenuate to the equilibrium value in the length of the computational domain. The maximum particle Reynolds number of 49 for the 20 μm case (vs. a maximum of 2.7 for the 2.4 μm drop), occurs just after the shock impacts the droplet-laden region. The corresponding maximum Weber number was approximately 6, indicating that droplets larger than 20 μm or shocks of higher strength may require a breakup model. At the other extreme, the smaller drop sizes (e.g., 5 μm or less) can have noncontinuum effects (e.g., $Kn_p > 0.01$) as they evaporate as shown in Table 2 for pre- and postshock conditions for the three initial diameters tested as well as for two smaller diameters that occur further behind the shock wave due to evaporation. These rarefaction effects can be significant to the drag force. For example, the correction to the drag coefficient for a 0.5 μm droplet corresponds to about a 25% reduction, while that of a 0.1 μm droplet corresponds to about a 70% reduction.

The gas temperature for each initial-diameter case is shown in Fig. 12b with comparison to the single-phase predictions. The simulations have the same temperature in the shocked region to the left of any droplets ($x < 0.3$ m) with a value that is consistent with the mixed-fluid theory value of 321 K for this mass loading. However, the gas-temperature increase due to the shock is substantially less than the unladen value due to energy transfer to the drops, especially for the smallest drop size, and occurs at a reduced x value due to shock speed attenuation. As the drop size increases, the total droplet surface area decreases (for a fixed mass loading) and this reduces the interphase heat transfer rate to the drops [Eq. (8)]. As such, the shock spike for the 2.4 μm case is replaced by a more gradual temperature increase for the 20 μm case. The increased time for coupling effects to occur for larger particles [Eq. (29b)] also yields an increased travel distance for the leading edge of the shock front as well as a local maximum in temperature. Another droplet size effect can be seen at around $x = 0.25$ m. In the case of the smaller particles, the gas reaches an equilibrium temperature once relative humidity reaches 100% and evaporation stops (for 0.3 m $< x <$ 0.6 m). For the largest particle diameter, the gas shows a slower and continued drop, because the droplets have not fully evaporated.

E. Effects of Specific Heat Ratio and of Evaporation

To investigate the effects of specific heats (since these can vary significantly among liquids and the gases of interest), two droplet specific heat ratios (c_s^*) of 4.17 and 1.0 were studied for a mass loading of 0.63, a drop diameter of 2.4 μm, and an initial shock Mach number of 1.25. The first specific heat ratio (4.17) matches that of liquid water, while the second (1.0) is more consistent with previous idealizations of dusty gases and is roughly consistent with liquid fuel in a fuel–air mixture. For these two ratios, the effects of interphase heat and mass transfer were examined by considering both conventional evaporation and artificial conditions without evaporation ($\dot{m} = 0$), which would behave more similar to solid-particle conditions. Shock attenuation results for each condition are shown in Fig. 13a with comparison to equilibrium theory. For $c_s^* = 4.17$, the mixed-fluid theoretical equilibrium shock Mach number is 0.89, while a slightly higher value of 0.93 occurs for $c_s^* = 1.0$. There is good agreement with mixed-fluid theory for the simulated cases without evaporation, but predictions with evaporation (especially with $c_s^* = 1.0$) fall slightly below the mixed-fluid value. This may be

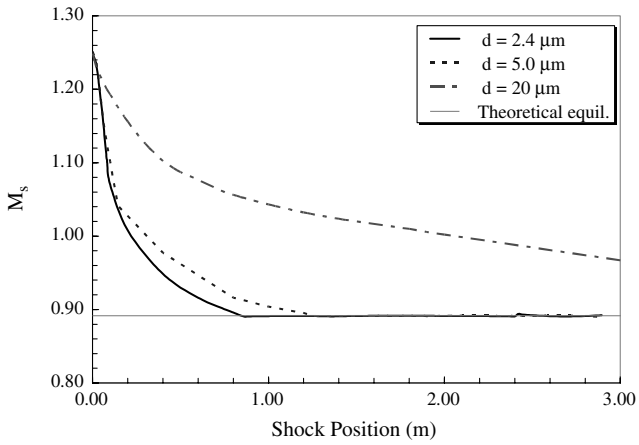

a)

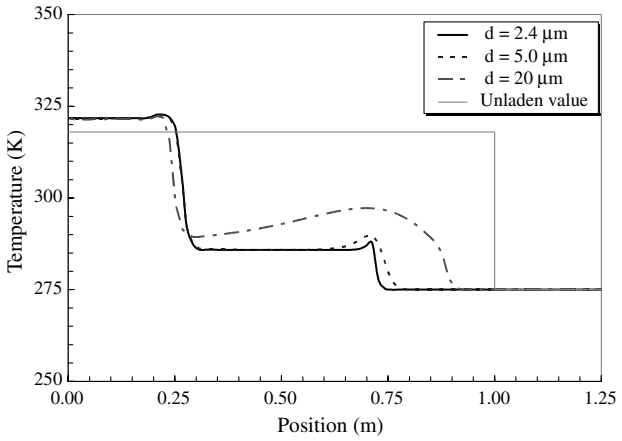

b)

Fig. 12 Plots of a) evolution of shock strength as a function of position for a range of drop diameters at a mass loading of 0.63 for case study 3 (theoretical equilibrium value from mixed-fluid theory is shown for comparison) and b) instantaneous gas-temperature comparison for various drop sizes at a loading of 0.63 for case study 3.

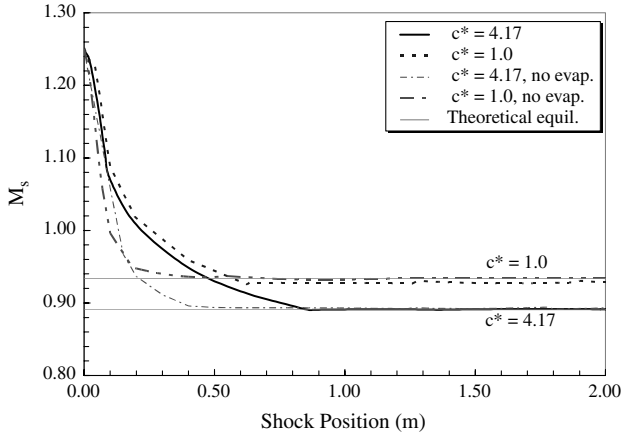

a)

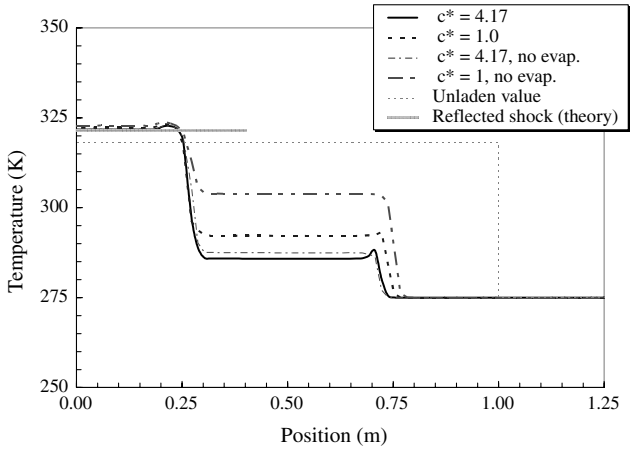

b)

Fig. 13 Plots of a) evolution of shock strength as a function of position for $c_s^* = 1.0, 4.17$ at a mass loading of 0.63 with and without evaporation effects for case studies 4 and 5, including theoretical mixed-fluid equilibrium shock Mach numbers and b) instantaneous gas-temperature spatial distributions for $c_s^* = 1.0, 4.17$ at a mass loading of 0.63, with and without evaporation for case studies 4 and 5.

attributed to the change in the gas species composition because of the addition of water vapor. The effects of evaporation are more substantial with respect to the rate of attenuation, whereby the distance to reach equilibrium is significantly increased in the evaporating case. This trend was unexpected by the authors (Kersey et al. [16]), since the evaporating case contains droplets that become smaller (and thus have shorter inertia response times on average) and since evaporation yields a larger relative temperature (and thus yields a higher thermal load on the gas). However, it can be explained by Eq. (29), which indicates that the gas-temperature response time ($\tau_{T,g}$) actually increases as the particle diameter decreases for a given number of particles per unit volume: i.e., a given mass loading.

The gas-temperature distributions shown in Fig. 13b further explain the effects of specific heat ratio and the importance of evaporation. As c_s^* increases for no evaporation, the associated increased thermal loading of the particles on the gas translates to a reduced local temperature rise behind the shock due to the reduced shock strength (noted in Fig. 13a). As evaporation is included for $c_s^* = 1$, the equilibrium gas temperature behind the shock reduces further due to the thermal energy required for phase change (recall from Fig. 6b that the droplet temperature reduces to the wet-bulb temperature during evaporation). This effect is less pronounced for $c_s^* = 4.17$, since particle heating dominates the thermal loading at this condition. As such, the effects of evaporation and specific heat ratio (like that of shock strength, particle size and mass loading) can impact the shock physics in a variety of ways.

IV. Conclusions

A numerical formulation was developed to handle finite rate interphase mass, momentum, and energy coupling and the scheme was evaluated with analytical and experimental conditions for both one-way and two-way coupling and for both low-speed and high-speed conditions. Simulations of shock attenuation by solid particles agreed reasonably well with data and previous numerical studies. Using this methodology, a parametric study of shock attenuation by small evaporating drops was conducted.

First, the effects of shock Mach number were studied at very low mass loadings (0.5%). At this condition, momentum effects were small as indicated by small relative velocities and a weak impact on shock speed. However, substantial changes in the gas temperature due to mass and heat transfer effects occurred even for this small mass loading due to the drop in particle temperature to the wet-bulb value behind the shock. At the interrogated time, the faster evaporation at the higher Mach number created a region with constant gas temperature where all the local drops had fully evaporated. In both cases, evaporation rates behind the shocks compared very well with experimental data by Goossens et al. [3].

Increased mass loading reduces the equilibrium shock Mach number and gas temperature rise due to momentum coupling effects, high loadings also increased the rate of shock attenuation due to a reduction in the thermal time scale [Eq. (29)]. The laden–unladen interface also caused a significant reflected shock in the opposite direction, which increased gas temperature in the shocked clean air region as compared to the unladen case, despite the stronger upstream thermal coupling. The strengths of the reflected shock and of the transmitted shock at equilibrium compared well with theory even when evaporation was included. However, evaporation effects led to complex gas-temperature profiles.

A study of the effect of droplet diameter indicated that larger drops take longer to reach postshock equilibrium conditions due to increased inertia. Examination of Knudsen numbers indicates that the drag coefficient can have significant rarefaction effects when the droplets evaporate postshock to submicron size. Higher specific heat ratios (consistent with higher thermal loadings) were found to reduce the equilibrium shock Mach number consistent with mixed-fluid theory. Interestingly, evaporation was found to slow the shock attenuation and reduce the postshock gas temperature. Future studies should consider the additional effects of droplet breakup, internal temperature variations, and combusting flow.

References

[1] Lu, H. Y., and Chiu, H. H., "Dynamics of Gases Containing Evaporable Liquid Droplets Under a Normal Shock," *AIAA Journal*, Vol. 4, No. 6, 1966, pp. 1008–1011. doi:10.2514/3.3595

[2] Panton, R., and Oppenheim, A. K., "Shock Relaxation in a Particle-Gas Mixture with Mass Transfer Between Phases," *AIAA Journal*, Vol. 6, No. 11, 1968, pp. 2071–2077. doi:10.2514/3.55431

[3] Goossens, H. W. J., Cleijne, J. W., Smolders, H. J., and van Dongen, M. E. H., "Shock Wave Induced Evaporation of Water Droplets in a Gas-Droplet Mixture," *Experiments in Fluids*, Vol. 6, 1988, pp. 561–568.

[4] Sommerfeld, M., "The Unsteadiness of Shock Waves Propagating Through Gas-Particle Mixtures," *Experiments in Fluids*, Vol. 3, No. 4, 1985, pp. 197–206.

[5] Haylett, R., Lappas, P. P., Davidson, D. F., and Hanson, R. K., "Application of an Aerosol Shock Tube to the Measurement of Diesel Ignition Delay Times," *Proceedings of the Combustion Institute*, Vol 32, No. 1, 2009, pp. 477–484. doi:10.1016/j.proci.2008.06.134,

[6] Hanson, T. C., Davidson, D. F., and Hanson, R. K., "Shock Tube Measurements of Water and *n*-Dodecane Droplet Evaporation behind Shock Waves," 43th AIAA Aerospace Sciences Meeting and Exhibit, Reno NV, AIAA Paper 2005-530, Jan. 2005.

[7] Sivier, S. A., Loth, E., Baum, J. D., and Lohner, R., "Unstructured Adaptive Remeshing Finite Element Method for Dusty Shock Flows," *Shock Waves*, Vol. 4, No. 1, 1994, pp. 31–41.

[8] Haselbacher, A., Najjar, F. M., Balachandar, S., and Ling, Y., "Lagrangian Simulations of Shock-Wave Diffraction at a Right-Angled

Corner in a Particle-Laden Gas," *6th International Conference on Multiphase Flow*, Leipzig, Germany, July 2007.

[9] Chang, E. J., and Kailasanath, K., "Shock Wave Interactions with Particles and Liquid Fluid Droplets," *Shock Waves*, Vol. 12, No. 4, 2003, pp. 333–342. doi:10.1007/s00193-002-0170-1

[10] Kersey, J., "Simulation of Shock Attenuation by Particles and Drops," M.S. Thesis, Aerospace Engineering Dept., Univ. of Illinois at Urbana–Champaign, Urbana, IL, 2007.

[11] Ranz, W. E., and Marshall, W. R., "Evaporation from Drops," *Chemical Engineering Progress*, Vol. 48, 1952, pp. 141–146.

[12] Loth, E., "Compressibility and Rarefaction Effects on Drag of a Spherical Particle," *AIAA Journal*, Vol. 46, No. 9, 2008, pp. 2219–2228. doi:10.2514/1.28943

[13] Stadler, J. R., and Zurick, V. J., "Theoretical Aerodynamic Characteristics of Bodies in Free-Molecule Flow Field," NACA TN 2423, July 1951, p. 12.

[14] Barton, E., "Exponential-Lagrangian Tracking Schemes Applied to Stokes Law," *Journal of Fluids Engineering*, Vol. 118, No. 1, 1996, pp. 85–89. doi:10.1115/1.2817520

[15] Lee, V., and Loth, E., "Local Adaptive Timestepping for Lagrangian Particle Tracking," 45th AIAA Aerospace Sciences Meeting, AIAA Paper 2007-335, Reno NV, Jan. 2007.

[16] Kersey, J., Loth, E., and Lankford, D., "Effect of Evaporating Drops on Shock Attenuation," 46th AIAA Aerospace Sciences Meeting and Exhibit, AIAA Paper 2008-793, Reno NV, Jan. 2008.

[17] Bush, R., Power, G., and Towne, C., "WIND-The Production flow solver of the NPARC Alliance," 36th AIAA Aerospace Sciences Meeting and Exhibit, Reno, NV, AIAA Paper 1998-0935, 1998.

[18] Bush, R., "A Three Dimensional Zonal Navier–Stokes Code for Subsonic Through Hypersonic Propulsion Flowfields," 24th AIAA/ASME/SAE/ASEE Joint Propulsion Conference, AIAA Paper 1988-2830, Boston, 1988.

[19] Koren, B., "A Robust Upwind Discretisation Method for Advection, Diffusion and Source Terms," *Numerical Methods for Advection-Diffusion Problems*, Notes on Numerical Fluid Mechanics, Vol. 45, Vieweg, Braunschweig, Germany, 1993, pp. 117–138.

[20] Amsden, A., O'Rourke, P., and Butler, T., "KIVA-II: A Computer Program for Chemically Reactive Flows with Sprays," Los Alamos National Lab., Rept. LA-11560-MS, Los Alamos, NM, 1989.

[21] Willbanks, C. E., and Schulz, R. J., "Analytical Study of Icing Simulation for Turbine Engines in Altitude Test Cells," Arnold Engineering Development Center, Rept. AEDC-TR-73-144, Arnold AFB, TN, 1973.

[22] Miura, H., and Glass, I. I., "On a Dusty-Gas Shock Tube," *Proceedings of the Royal Society of London A*, Vol. 382, No. 1783, 1982, pp. 373–388. doi:10.1098/rspa.1982.0107

[23] Eaton, J. K., and Fessler, J. R., "Preferential Concentration of Particles by Turbulence," *International Journal of Multiphase Flow*, Vol. 20, 1994, pp. 169–209. doi:10.1016/0301-9322(94)90072-8

[24] Aliseda, A., Cartellier, A., Hainaux, F., and Lasheras, J. C., "Effect of Preferential Concentration on the Settling Velocity of Heavy Particles in Homogeneous Isotropic Turbulence," *Journal of Fluid Mechanics*, Vol. 468, 2002, pp. 77–105. doi:10.1017/S0022112002001593

J. Gore
Associate Editor